Eur. Phys. J. D (2013) 67: 248
DOI: 10.1140/epjd/e2013-40489-2

THE EUROPEAN PHYSICAL JOURNAL D

Regular Article

Regular and chaotic dynamics of a neutral atom in a magnetic trap

Jose Pablo Salas[a] and Manuel Iñarrea

Departamento de Química, Área de Física Aplicada, Universidad de La Rioja, 26006 Logroño, Spain

Received 9 August 2013 / Received in final form 26 September 2013
Published online 3 December 2013 –

Abstract. In the framework of the nonlinear mechanics, we study the dynamics of a neutral atom confined in a magnetic quadrupolar trap. Owing to the axial symmetry of the system, the z-component of the angular momentum p_ϕ is an integral of motion and, in cylindrical coordinates, the dynamics of the atom is modeled by a two-degree of freedom Hamiltonian. The structure and evolution of the phase space as a function of the energy is explored extensively by means of numerical techniques of continuation of families of periodic orbits and Poincaré surfaces of section.

1 Introduction

In the last decade of the 20th century, the experimental achievement of Bose-Einstein condensation (BEC) of atoms has turned one of the most beautiful physics dreams into reality [1–5]. Today, BEC remains one of the most active fields in physics in such way that it would imposible to enumerate the phetora of experimental and theoretical papers related to BEC. A Bose-Einstein condensate is obtained when a gas of bosonic neutral atoms are led below a critical temperature of a few tens of nanokelvins from which, most of the atoms are occupying the same quantum state.

Cooling atoms to those very low critical temperatures was a technical challenge that required the development of several experimental techniques [6]. The first one was laser cooling [7–9] and with this procedure, atoms are cooled to temperatures in the microkelvin range. In any case, these temperatures are not low enough to obtain atomic condensates and it is necessary to further reduce the temperature of the atoms by evaporative cooling [10,11]. However, before to be evaporatively cooled, atoms have to be confined in a magnetic trap. For this reason, magnetic trapping is a crucial step in the BEC attainment.

The magnetic confining of neutral atoms with permanent magnetic moment is possible due to the interaction of the magnetic moment with a non-uniform static magnetic field. In order to be trapped, the magnetic force on the atom must be attractive and it requires the magnetic moment and the field to keep an appropriate relative direction. This takes place when the Larmor precession frequency of the magnetic moment around the field is much greater than the orbital frequency. Under this approximation (the so-called adiabatic condition), the orbital motion does not affect the relative orientation between the magnetic moment and the local field. In this way, the atom keeps the desired orientation in a fixed positive Zeeman sublevel and the trapping takes place around a local minimum of the field [4]. If the adiabatic condition breaks, the force may become repulsive due to magnetic moment flips to untrapped negative Zeeman sublevels, in such way that the atom is ejected from the trap. These spin flips (Majorana transitions [12]) are likely to occur in trap regions where the atom is moving fast and where the field strength is small [13].

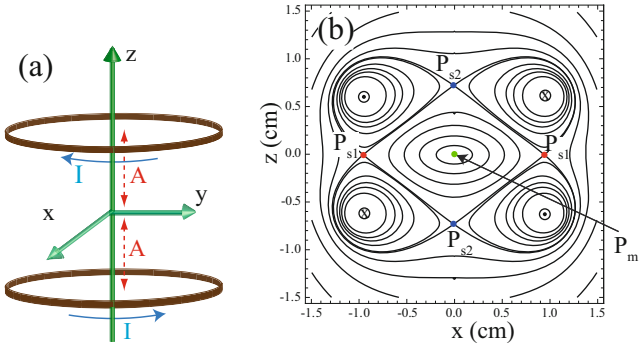

Fig. 1. (a) Two-coils quadrupole magnetic trap. (b) Contour levels of $B(\rho, z; A)$ along the direction $y = 0$. All contours are plotted at every 20 G up to 200 G except the contour passing through the saddle points at 97.4327 G.

The quadrupole trap [14–16] and the Ioffe trap [14,17] are among the most significant magnetic traps for neutral atoms. The quadrupole trap consists of two Helmholtz coils with currents in opposite directions (see Fig. 1). The field at the center of this trap has a zero minimum. The Ioffe trap consists of four straight currents bars plus two Helmholtz coils and it has a non-zero field minimum. The theory of confining magnetic fields for neutral atoms is developed in [14]. In that paper, the cumbersome exact expressions of the magnetic field are replaced by suitable

[a] e-mail: josepablo.salas@unirioja.es

multipole polynomial expansions. As it is pointed in that paper, these multipole expansions would be useful for quantum and classical calculations.

The relevance of studying the classical dynamics of magnetically trapped neutral species for atom spectroscopy was pointed out by several authors [18–20]. Nevertheless, classical studies have been surprisingly relegated. The main classical approaches are now briefly summarized. A seminal study by Bergeman [5,21,22] showed that, for high enough energy, the classical dynamics of an atom trapped in a quadrupolar trap is chaotic. Later on, Gomer et al. [18] found similar results. It is worth noting that these works were performed using only the first non-trivial terms of the multipole polynomial expansion of the magnetic field. Surkov et al. [23] studied the low energy coupling between the three-degree of freedom of an atom in a Ioffe trap.

The main goal of this paper is to cover the lack of classical studies in magnetically trapped neutral atoms. Thence, we pay attention in the classical dynamics of an atom trapped in a quadrupole trap. Finally, we point here that the highly non-linear nature of the trapping magnetic fields, makes these systems very attractive for their classical study.

The paper is organized as follows. In Section 2, we use the adiabatic approximation to state the confining potential created by the quadrupolar trap. In Section 3 we establish the two-degree of freedom Hamiltonian governing the dynamics of the system. By using a convenient set of units, we obtain that the relevant parameters controlling the dynamics are the z-component p_ϕ of the angular momentum and the energy E. The study of the critical points of the effective potential of the system is provided in Section 4. From this study, we can understand part of the dynamics. In Section 5 and 6 we study, for two different values of p_ϕ, the evolution of the phase space structure of the system as a function of the energy E. In particular, in Section 5, we perform a comprehensive study of the bifurcations of the two fundamental families of periodic orbits (normal modes) that determine the phase space structure. The escape dynamics is also studied in Sections 5 and 6. The conclusions are provided in Section 7.

2 The confining potential

Under the adiabatic approximation, the atom remains in a fixed Zeeman sublevel m_F and the potential $V(r)$ responsible for the interaction between the atom and the magnetic field $\boldsymbol{B}$ is given by [4]

$$V(r) \approx \mu_{ef}\ B(r), \quad \mu_{ef} = \mu_B\ g\ m_F, \tag{1}$$

where g is the g-factor and μ_B is the Bohr magneton. From equation (1) we observe that trappable states are those with positive $m_F > 0$ (low-field seeking states) [4].

Now, let us consider a two coils magnetic quadrupole trap. The coils, of radius R and with opposite equal currents I, are perpendicular to the z axis and centered at $z_o = \pm A$ (see Fig. 1a). The axial z-symmetry of the magnetic field created by a coil makes convenient to use cylindrical coordinates (ρ, z, ϕ). In this way, the azimuthal B_ϕ, axial B_z and radial B_ρ components of the magnetic field of each coil are given by [14,24]

$$B_\phi = 0, \tag{2}$$

$$B_z = \frac{\mu_o\ I}{2\ \pi}\ b_z(\rho, z; z_o), \tag{3}$$

$$B_\rho = \frac{\mu_o\ I}{2\ \pi}\ b_\rho(\rho, z; z_o), \tag{4}$$

where the terms $b_z(\rho, z; z_o)$ and $b_\rho(\rho, z; z_o)$ are the expressions:

$$b_z(\rho, z; z_o) = \frac{1}{\sqrt{(R+\rho)^2 + (z-z_o)^2}} \tag{5}$$

$$\times \left[K(k^2) + \frac{R^2 - \rho^2 - (z-z_o)^2}{(R-\rho)^2 + (z-z_o)^2}\ E(k^2)\right], \tag{6}$$

$$b_\rho(\rho, z; z_o) = \frac{z - z_o}{\rho\ \sqrt{(R+\rho)^2 + (z-z_o)^2}} \tag{7}$$

$$\times \left[-K(k^2) + \frac{R^2 + \rho^2 + (z-z_o)^2}{(R-\rho)^2 + (z-z_o)^2}\ E(k^2)\right], \tag{8}$$

being $k^2 = 4\ R\ \rho / \left[(R+\rho)^2 + (z-z_o)^2\right]$ the argument of the complete elliptic integrals K and E. Using the expressions (2)–(7) for our two coils trap configuration and according to expression (1), the confining potential $V(\rho, z; A)$ is given by

$$V(\rho, z; A) = \mu_{ef}\ B(\rho, z; A) \tag{9}$$

$$B(\rho, z; A) = \frac{\mu_o\ I}{2\ \pi}\ \Big[\left[b_\rho(\rho, z; A) - b_\rho(\rho, z; -A)\right]^2 + \left[b_z(\rho, z; A) - b_z(\rho, z; -A)\right]^2\Big]^{1/2}. \tag{10}$$

Note that $V(\rho, z; A)$ is also symmetric with respect to the coordinate z. Except for the value of μ_{ef}, $V(\rho, z; A)$ and $B(\rho, z; A)$ present the same landscape with four critical points: a minimum P_m of zero value at the origin and three saddle points (see Fig. 1b). The existence of the minimum provides the confining ability. One of the saddles (P_{s1} in Fig. 1b) is located at the $z = 0$ axis. The other two saddle points, named P_{s2}, have equal same threshold value and they are symmetrically located at the $\rho = 0$ axis (see Fig. 1b). For $A/R = 0.62673$ all the saddle points have the same energy. This is the depicted situation in Figure 1b.

The usual approach to study the dynamics of atoms moving near the center of the trap is to consider the first term $V_1(\rho, z; A)$ of the multipole polynomial expansions of $V(\rho, z; A)$ [14]. This term is given by:

$$V_1(\rho, z; A) = \mu_{ef}\ B_1(\rho, z; A), \tag{11}$$

$$B_1(\rho, z; A) = b_1\ \sqrt{\rho^2 + 4z^2}, \qquad b_1 = \frac{3\ I\ A\ R^2\ \mu_o}{2\ (R^2 + A^2)^{5/2}}.$$

We study the accuracy of this approximation in Figure 2 by comparing the contour magnetic field lines given by (11) to the exact contour field lines given by (9). As it

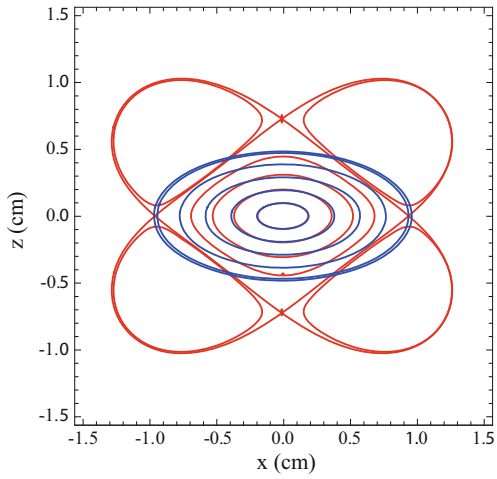

Fig. 2. Comparisson between the contour levels (blue curves) of $B_1(\rho, z; A)$ from the expansion (11) and the contour levels (red curves) of $B(\rho, z; A)$ from the exact expression (10). Contours for 20 G, 40 G, 60 G, 80 G, 97.4327 G and 100 G. Figure for $I = 200$ A, $R = 1$ cm and $A = 0.62673$ cm.

was expected, this short expansion behaves correctly near the center of the trap.

In a conventional trap of a few centimeters in size, b_1 (the field gradient) is about a few hundred Gauss/cm. In particular, $b_1 \approx 100$ G/cm for $R = 1$ cm, $A = 0.62673$ cm and $I = 200$ A. If the atom is sodium in the $m_F = 2$ Zeeman sublevel, and the circular orbit has a radius $\rho_o = 0.1$ cm, we get $\omega_L/2\pi \approx 55$ MHz and $\omega/2\pi \approx 150$ Hz. Thence, the adiabatic condition is fulfilled and the motion of the atom can be considered classical.

3 The Hamiltonian and reductions

In cylindrical coordinates, the Hamiltonian $\mathcal{H}$ of a trapped atom of mass m reads as

$$\mathcal{H} = \frac{1}{2m}\left(p_\rho^2 + p_z^2 + \frac{p_\phi^2}{\rho^2}\right) + V(\rho, z; A). \qquad (12)$$

Due to the axial symmetry of the field, the z-component p_ϕ of the angular momentum is a constant of the motion, and we are dealing with a two-degree of freedom Hamiltonian system. We define the effective potential

$$U(\rho, z; A) = p_\phi^2/(2m\rho^2) + V(\rho, z; A)$$

which includes the centrifugal term depending on p_ϕ. Besides the internal parameters p_ϕ and the energy $\mathcal{H} = E$, the dynamics depends on the external parameters m, μ_{ef}, I, R, A, that is to say, on the kind of atom and on the geometry of the trap. It is possible to reduce the number of the external parameters by using the dimensionless lengths $\rho' = \rho/R$, $z' = z/R$ and $A' = A/R$ and the dimensionless time $t' = t\,\omega_o$, where the frequency ω_o is

$$\omega_o = \sqrt{\frac{\mu_{ef} B_o}{mR^2}}, \qquad B_0 = \frac{\mu_o\, I}{2\,\pi\, R}.$$

Applying these transformations to (12), we arrive at the following dimensionless Hamiltonian

$$E' = \mathcal{H}' = \frac{\mathcal{H}}{\mu_{ef}\ B_o} = \frac{1}{2}\left(p_\rho'^2 + p_z'^2\right) + U(\rho', z'; A'), \quad (13)$$

where the (dimensionless) effective potential takes the form

$$U(\rho', z'; A') = \frac{p_\phi'^2}{2\rho'^2} + \Big[\left[b_{\rho'}(\rho', z'; A') - b_\rho(\rho', z'; -A')\right]^2 + \left[b_z(\rho', z'; A') - b_z(\rho', z'; -A')\right]^2\Big] 1/2. \qquad (14)$$

Now, the system depends on the three parameters (E', p_ϕ', A'). Note that the energy E' is expressed in units of $E_o = \mu_{ef}\ B_o$. If the same procedure is applied to the expansion (11), we get

$$U_1(\rho', z'; A') = \frac{p_\phi'^2}{2\rho'^2} + b_1'\sqrt{\rho'^2 + 4z'^2}, \quad b_1' = \frac{3\ A'\ \pi}{(1 + A'^2)^{5/2}}. \qquad (15)$$

In order to simplify the notation, hereafter we drop primes in coordinates and momenta. From Hamiltonian (13), the equations of motion read as

$$\dot{z} = p_z, \qquad \dot{\rho} = p_\rho,$$
$$\dot{p}_z = -\frac{\partial V(\rho, z; A')}{\partial z}, \qquad \dot{p}_\rho = \frac{p_\phi^2}{\rho^3} - \frac{\partial V(\rho, z; A')}{\partial \rho}. \qquad (16)$$

If we consider initial conditions with $p_z = z = 0$, it is easy to check that in the equations of motion (16) we obtain $\dot{p}_z = \dot{z} = 0$, which corresponds to pure analytic vibrational rectilinear periodic orbits along the ρ axis. We name this kind of rectilinear orbits as I_ρ.

4 The effective potential

A previous way to understand the dynamics is to study the shape of the effective potential $U(\rho, z; A')$. The shape of $U(\rho, z; A')$ is mainly determined by its critical points. The critical points of $U(\rho, z; A')$ are given by the solutions of the equations

$$\frac{\partial V(\rho, z; A')}{\partial z} = 0,$$
$$\frac{p_\phi^2}{\rho^3} - \frac{\partial V(\rho, z; A')}{\partial \rho} = 0. \qquad (17)$$

For a constant value of A' (fixed trap geometry), the position and the energy of the critical points depend on p_ϕ. In what follows, we take $A' = 0.62673$. For $p_\phi = 0$, the critical points of $U(\rho, z; A')$ are those of $V(\rho, z; A')$, e.g., the minimum P_m and the saddle points P_{s1} and P_{s2} showed in Figure 1b. When $p_\phi \neq 0$, the centrifugal barrier in $U(\rho, z; A')$ prevents the atom to cross the center of the trap, and the minimum P_m and the saddle points P_{s2} are shifted from the $\rho = 0$ axis (see Fig. 3a for $A' = 0.62673$

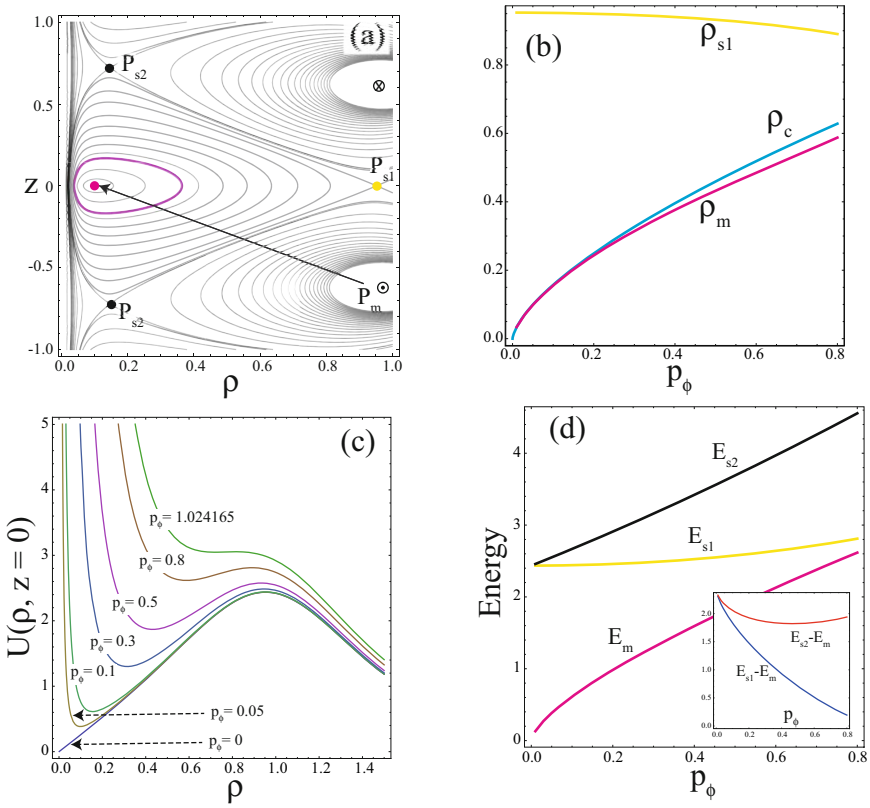

Fig. 3. (a) Equipotencial curves of the effective potencial $U(\rho, z; A')$ for $p_\phi = 0.05$. The purple colored curve stands for the (dimensionless) energy $E = 1$ contour. (b) Evolution as a function of p_ϕ of the positions of ρ_m, the characteristic radius ρ_c and the saddle point P_{s1}. (c) Effective potential along the $z = 0$ direction for increasing values of p_ϕ. As p_ϕ increases the depth of the potential well along the ρ direction decreases and eventually it disappears. (d) Evolution as a function of p_ϕ of the energy (E_m, E_{s1}, E_{s2}) of the critical points (P_m, P_{s1}, P_{s2}). All figures for $A' = 0.62673$.

and $p_\phi = 0.05$). When the atom is moving near the center of the trap, we use the approximation $V_1(\rho, z; A')$ given by the expression (15) to get that the minimum P_m is located at the characteristic radius ρ_c,

$$\rho_c = \left(\frac{p_\phi^2}{b_1'}\right)^{1/3}. \tag{18}$$

The evolution of (18) as a function of p_ϕ is shown in Figure 3b. However, in the general case it is not possible to obtain close expressions of the critical points as a function of p_ϕ. Hence, we obtain the position and the energy of the critical points by solving numerically equations (17) for different values of p_ϕ. In Figure 3b is depicted the evolution of ρ_m and ρ_{s1} in the interval $0 \leq p_\phi \leq 0.8$, where ρ_m and ρ_{s1} are, respectively, the positions of the minimum P_m and the saddle point P_{s1} at the ρ axis. For increasing p_ϕ, Figures 3b–3c show that the minimum P_m moves away from the center of the trap. At the same time, the saddle point P_{s1} approaches the minimum P_m in such way that at $p_\phi \approx 1.02416$ they collide and both disappear (this situation is showed in Fig. 3c). As consequence, for $p_\phi > 1.02416$, there is not potential well and the atom can not be confined. For a wide range of values of p_ϕ, Figure 3b shows that the characteristic radius ρ_c is a very good approximation of ρ_m. Roughly speaking, through the value of p_ϕ, equation (18) allows us to control the "mean" size ρ_c of the orbits that the trapped atom can describe, e.g., p_ϕ indicates how far from the center of the trap the atom can be orbiting.

The evolution of the energies E_m, E_{s1} and E_{s2} of the critical points P_m, P_{s1} and P_{s2} in the same p_ϕ interval is shown in Figure 3d. In the inset of this figure it is also shown the evolution of the potential well depth by plotting the energy gaps $(E_{s1} - E_m)$ and $(E_{s2} - E_m)$. For $p_\phi \neq 0$, the energies E_{s1} and E_{s2} are no longer equal, being $E_{s1} < E_{s2}$ and E_{s2} increases much faster than E_{s1}. Indeed, the escape channel along P_{s1} (e.g. along the ρ axis) is energetically more accessible than the channel along P_{s2}. In other words, the energy E_{s1} determines the potential well depth of the trap. As expected, when p_ϕ increases, the energies E_m and E_{s1} tend one to each other in such way that, at $p_\phi \approx 1.02416$ when ρ_m and ρ_{s1} collide, we have that $E_m \approx E_{s1}$.

5 Phase space structure

In the preceding Section 2, we concluded that p_ϕ controls the confining ability of the trap. In this section we will study the evolution of the phase phase governed by the Hamiltonian (13) as a function of the parameters p_ϕ and E.

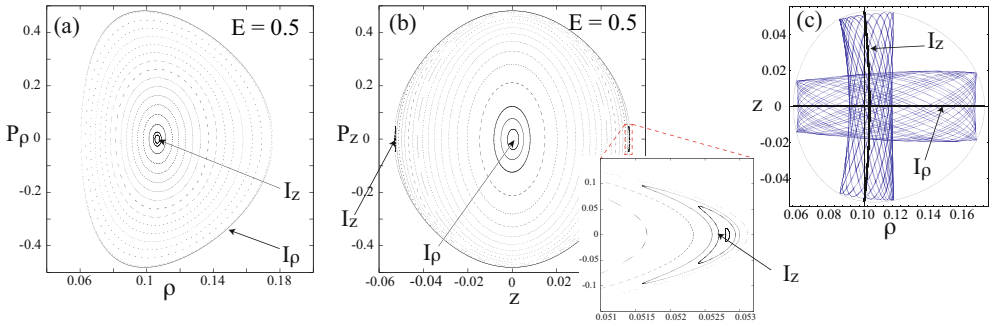

Fig. 4. Surfaces of section (a) $p_z = 0$ and (b) $p_\rho = 0$. (c) Normal modes I_z and I_ρ and examples of quasiperiodic orbits around them. All figures for $p_\phi = 0.05$ and energy $E = 0.5$.

The phase space structure of a two-degress of freedom Hamiltonian system is mainly characterized by the number and stability of the periodic orbits existing in phase space. A common way to illustrate the structure and evolution of the phase space of a two-degree of freedom Hamiltonian system is by using Poincaré surfaces of section. In our problem there are two ways to define a convenient surface of section. One of them as the intersection of the phase trajectories with the (ρ, p_ρ) plane for $p_z = 0$, and the other as the intersection of the phase trajectories with the (z, p_z) plane for $p_\rho = 0$. The $p_z = 0$ and the $p_\rho = 0$ Poincaré maps will provide a complementary vision of the phase space structure because we can ensure that all orbits will cross at least one of them at any time. Taking into account the symmetry of the potential $V(\rho, z; A')$ with respect to the z axis, the limit of the available region of the surface of section $p_z = 0$ in the plane (ρ, p_ρ) is determined by the possible values of the momentum p_ρ that are given by the equation

$$p_\rho = \pm\sqrt{2\left[E - \frac{p_\phi^2}{\rho^2} - V(\rho, z = 0; A')\right]}. \qquad (19)$$

It is worth noting that the rectilinear orbits I_ρ are tangent to the phase flux in this $p_z = 0$ Poincaré map and they correspond to the curves defined by (19). On the other side, the available region of the $p_\rho = 0$ surface of section in the plane (z, p_z) is determined by those values of p_z satisfying

$$p_z = \pm\sqrt{2\left[E - \frac{p_\phi^2}{\rho^2} - V(\rho, z; A')\right]}. \qquad (20)$$

Therefore, the limit of the $p_\rho = 0$ Poincaré map corresponds to the maximum and minimum values of p_z satisfying equation (20).

The dynamics of the systems depends on the parameters p_ϕ and E. The range of variation of the energy E is largely determined by p_ϕ because its value regulates the effective potential well depth and the mean size of the trapped orbits. Then, to study the evolution of the phase space structure we fix the value of p_ϕ while we vary the energy E. The choice of p_ϕ is a delicate task; it must be large enough to satisfy the adiabatic condition, while still small enough for the atom to be trapped (see Fig. 3c). Moreover, from a classical point of view, passages through the origin are a major drawback in the computation of orbits because in the quadrupolar trap the first derivatives of $V(\rho, z; A')$ at the origin are not continuous. This fact can be easily checked when the approach $V_1(\rho, z; A')$, equation (11), is used. Thence, in order to preserve the adiabatic condition and to avoid passages through the origin, we consider in this paper the general case of trajectories with values of $p_\phi \neq 0$. In particular, we choose in this study the values $p_\phi = 0.05$ and $p_\phi = 0.5$. These two p_ϕ values fulfill the adiabatic condition and at the same time they are sufficiently different from each other to assess the influence of p_ϕ on the dynamics. In this section we fix the value $p_\phi = 0.05$ while in Section 6, the value $p_\phi = 0.5$ is used.

For $p_\phi = 0.05$, the minimum of the effective potential is located at $\rho_m \approx 0.1$ and its energy is $E_m \approx 0.3841$. In Figures 4a and 4b we show the surfaces of section $p_z = 0$ and $p_\rho = 0$ for an energy $E = 0.5$. In these surfaces of section orbits are ordered forming invariant KAM tori around a central stable fixed point. Note that this is the expected phase space structure for energies close to the minimum energy E_m. The central fixed point in Figure 4a corresponds to the arch-like periodic orbit named as I_z in Figure 4c, while the central point in Figure 4b corresponds to I_ρ (see Fig. 4c). In the left and in the right sides of the $p_\rho = 0$ Poincaré section of Figure 4b we observe two small structures with two stable fixed points which correspond to I_z. Note that in the Poincaré map $p_\rho = 0$, I_z is almost tangent to the flux. In fact, for $p_\phi = 0$, I_z is an analytical rectilinear orbit along the z axis tangent to the $p_\rho = 0$ flux.

Indeed, at this energy, there only exist the two periodic orbits I_ρ and I_z which are the radial and the axial nonlinear normal modes of the system [25,26]. The phase space is organized around them in such way that, the nearer a quasiperiodic orbit is to I_z (I_ρ), the greater its orientation is along the periodic orbit I_z (I_ρ). Examples of quasiperiodic orbits around I_z and I_ρ are shown in Figure 4c. Roughly speaking, as long as I_z and I_ρ are the only periodic orbits, the system shows a quasi-linear behavior because its nonlinearity reduces to a smooth mixture of the normal modes I_z and I_ρ. In the low energy regime, a similar coupling between the axial and the radial degree

of freedom of an atom in a Ioffe trap was found by Surkov et al. [23].

5.1 The stability index k

It is well known that the linear stability of a periodic orbit of period T is determined from the eigenvalues of the monodromy matrix $M_1 = M(T)$. As we are dealing with a Hamiltonian system, the four eigenvalues $(\lambda_1, \lambda_2, \lambda_3, \lambda_4)$ of M_1 appear in reciprocal pairs. Following the invariance of the Hamiltonians equations of motion, we have two trivial eigenvalues $\lambda_1 = \lambda_2 = 1$. Thus, we just have to study the remaining two eigenvalues (λ_3, λ_4) of M_1. As they are complex conjugate and reciprocal, $\lambda = \lambda_3 = 1/\lambda_4$, they are on the unit circle in the complex plane or on the real axis. In order to have a stable periodic orbit, the two eigenvalues have to be on the unit circle [27]. If λ_3 and λ_4 are real the orbit is unstable. At the critical cases $\lambda_3 = \lambda_4 = \pm 1$ the stability may change. The stability index k is usually defined as [28]

$$k = \lambda + 1/\lambda = \mathrm{Tr}(\mathrm{M}_1) - 2.$$

Indeed, a periodic orbit is stable when $|k| < 2$, unstable when $|k| > 2$ and critical when $|k| = 2$. The critical values $k = \pm 2$ mean that a new family of periodic orbits has likely bifurcated from the original one. In particular, the critical value $k = 2$ is very important because families of periodic orbits always appear or disappear when the stability index takes that value [29]. In general, a periodic orbit of period mT ($m \in \mathbb{N}$) may bifurcate from a parent periodic orbit of period T when

$$k = 2\cos(2\pi\ n/m), \tag{21}$$

with $n \leq m$ coprime natural numbers [29].

There is a close connection between the number m and the multiplicity of a periodic orbit. We define the multiplicity m' of a T-periodic orbit as the number of fixed points that the orbit generates on a given Poincaré map. For example, I_z and I_ρ have multiplicity $m' = 1$ with respect to the Poincaré map $p_z = 0$. So, when a mT periodic orbit bifurcates from a parent T-periodic orbit of multiplicity m', the multiplicity of the bifurcated orbit is $m \cdot m'$. We will label the different families of periodic orbits with its multiplicity m.

Therefore, the combined use of Poincaré sections, numerical continuation of families of periodic orbits and stability diagrams, where k is plotted versus the parameter generator of the family, is a useful tool in nonlinear studies (see for instance [28,30–33]). At this point, we proceed as follows. For a fixed value of p_ϕ and by using the software AUTO [34], we carry out the numerical continuation of the families of the periodic orbits I_ρ and I_z that emanate from these solutions. For fixed p_ϕ, the only free parameter for our continuation procedure is the energy E, in such way that the stability diagram of each family as a function of the energy E is computed. From this diagram, we can detect values of the energy where possible bifurcations take place. Because a bifurcation produces qualitative changes in the phase space structure, we illustrate its effect by calculating the surfaces of section when the energy is slightly lower and slightly larger than the value at the bifurcation.

5.2 Bifurcations of the normal modes I_z and I_ρ

For $p_\phi = 0.05$, the energies of the saddle points P_{s1} and P_{s2} are $E_{s1} \approx 2.4372$ and $E_{s2} \approx 2.5503$. Then, we compute the evolution of the stability indexes k_z and k_ρ of the families I_z and I_ρ in the interval $0.5 \leq E \leq E_{s1}$. The result of this calculation is shown in Figure 5, where k_z and k_ρ are represented with black lines. A first look to Figure 5 shows the occurrence of several bifurcations. We will study some of them for increasing energy.

The I_ρ periodic orbit suffers the first bifurcation at $E \approx 0.5200$ (see Fig. 5b). At that energy and at $k_\rho = 2$, there appear two new branches, one stable and one unstable (solid and dashed green lines in Fig. 5b). Due to the slow evolution of the stability index of these families, to observe this bifurcation in the surfaces of section we have to move to energy values far from the bifurcation energy value, for example to $E = 1.8$. Because for this energy value, several bifurcations have taken place, we will illustrate it later. However, and as we will observe later, this is an island-chain bifurcation of multiplicity $m = 6$ because, at $E \approx 0.5200$, the stability index of I_ρ is $k \approx -1$, which corresponds to $m = 6$ in equation (21).

As we observe in Figure 5a, the I_z mode suffers the next two bifurcations because at $E \approx 0.5606$ and at $E \approx 0.6659$, the stability index k_z crosses twice the value $k_z = 2$. Both bifurcations are of pitchfork type and they are visualized in the $p_z = 0$ surfaces of section of Figure 6. For $E = 0.54$ (see Fig. 6a) the surface of section presents the same qualitative structure as Figure 4a. When the critical value $E \approx 0.5606$ is crossed, we observe in Figure 6b for $E = 0.58$ the pitchfork bifurcation: from the fixed point I_z (which becomes unstable) emanate two stable fixed points (periodic orbits) of multiplicity $m = 1$. These new two stable periodic orbits, which correspond to the green solid line in Figure 5a, consist of two symmetric arch-like shaped orbits, which are a mirror reflection of one another with regard to the ρ-axis (see Fig. 6d). The second pitchfork bifurcation is observed in Figure 6c. The periodic orbit I_ρ appears as a stable point surrounded by a heteroclinic separatrix passing through two unstable fixed points of multiplicity $m = 1$. Both unstable families are represented in Figure 5a with the same dashed blue line. These new unstable fixed points correspond to the same symmetric periodic orbit with regard to the ρ-axis but traveled in opposite senses (see Fig. 6d). After these two bifurcations, the quasi-linear behavior of the system is lost because there emerge new regions of motion different from the primal around I_z and I_ρ.

When the energy is $E \approx 1.0206$, we detect in diagram of Figure 5a the forth bifurcation because at $k_z = 2$ there appear two new branches, one stable and one unstable (solid and dashed magenta lines). Again, due to the slow evolution of the stability index of these families, we will illustrate this bifurcation later. Nevertheless, we

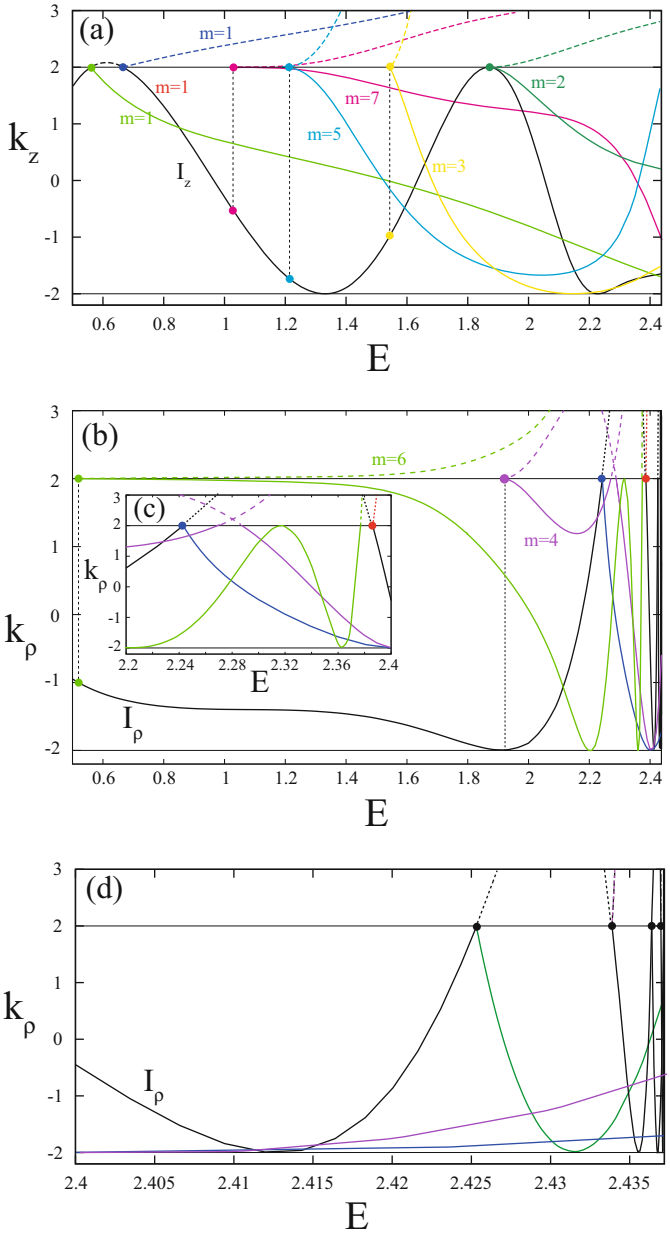

Fig. 5. Numerical continuation of the families of the periodic orbits arising from the normal modes I_z and I_ρ in the energy interval $0.5 \leq E \leq E_{s2}$. The upper diagram shows the evolution of the stability indexes k_z of the families of periodic orbits arising from I_z. The central and lower diagrams show the evolution of the stability indexes k_ρ of the families of periodic orbits arising from I_ρ. Dashed lines indicate instability. See the text for details.

point here that it is an island-chain bifurcation of multiplicity $m = 7$. We confirm this bifurcation because at $E \approx 1.0206$ the stability index of I_z is $k_z \approx -0.4450$, which corresponds to $m = 7$ in equation (21).

The next bifurcation is suffered by I_z and it takes place at $E \approx 1.1889$. At this energy value and at $k_z = 2$, there appear two new branches, one stable and one unstable (solid and dashed cyan lines in Fig. 5a). As we observe in the surface of section of Figure 7a for $E = 1.25$, this is an island-chain bifurcation of multiplicity $m = 5$ because there appears a resonance of five islands around I_z, which remains stable. The stable fixed point in the center of each of the five islands corresponds to the stable cyan branch in Figure 5a. The five islands are enclosed by a separatrix passing through five unstable fixed points, which correspond to the unstable dashed cyan branch in Figure 5a. The new stable periodic motion is represented in Figure 7b for $E = 1.25$. Again, we can ensure that it is island-chain bifurcation of multiplicity $m = 5$ because at the bifurcation energy $E \approx 1.1889$, the stability index of I_z is $k_z \approx 0.6180$, which corresponds to $m = 5$ in equation (21).

The normal mode I_z is also involved in the next bifurcation that takes place at $E \approx 1.5408$. At that energy, there appear at $k_z = 2$ two branches, one stable and one unstable (solid and dashed yellow lines in Fig. 5a). As we observe in the $p_z = 0$ surface of section in Figure 8a for $E = 1.75$, it is an island-chain bifurcation of multiplicity $m = 3$. Once again, equation (21) confirms this bifurcation. The new $m = 3$ stable periodic orbit is depicted in Figure 8b for $E = 1.75$.

At the energy $E = 1.75$, in the $p_z = 0$ surface of section of Figure 8a it is already possible to observe the $m = 7$ island bifurcation suffered by I_z at $E \approx 1.0206$ (magenta branches in Fig. 5a). At $E = 1.75$, in the $p_\rho = 0$ Poincaré section of Figure 8c, it is also possible to observe the $m = 6$ island bifurcation suffered by I_ρ at $E \approx 0.5200$ (green branches in Fig. 5b). The stable periodic orbits $m = 6$ and $m = 7$ are depicted in Figure 8d for $E = 1.75$.

We find the next bifurcation at $E \approx 1.8692$ when the estability index of I_z reaches the value $k_z = 2$. This is a double period-doubling bifurcation: from I_z there emerge four new periodic families, two stable and two unstable of multiplicity $m = 2$. The two new stable (unstable) families have the same stability index values, and therefore both families are represented in Figure 5 by the same solid (dashed) dark green line. In Figure 9a it is shown the $E = 2$ surface of section after that bifurcation, while in Figure 9b are depicted for the same energy the new stable periodic motions that emerge from this bifurcation. Note that the new stable periodic motions are mirror reflections of each other with respect the ρ-axis. The two unstable periodic orbits correspond to the same orbit but travelled in opposite senses. For simplicity, we do not represent the unstable orbits.

At $E \approx 1.9135$, the stability index of I_ρ reaches the critical value $k_\rho = -2$ while at the same energy value there appear at $k_\rho = 2$ two new branches (purple lines in Fig. 5b), one stable and one unstable. This is again an island-chain bifurcation of multiplicity $m = 4$ and thus, it is very similar to the previously studied. This bifurcation is visualized in the $p_\rho = 0$ Poincaré map for $E = 2$ of Figure 10a: around I_ρ there appears a resonance made of eight new fixed points, four stable and four unstable. The new $m = 4$ stable periodic orbit is drawn in purple color in Figure 10b for $E = 2$.

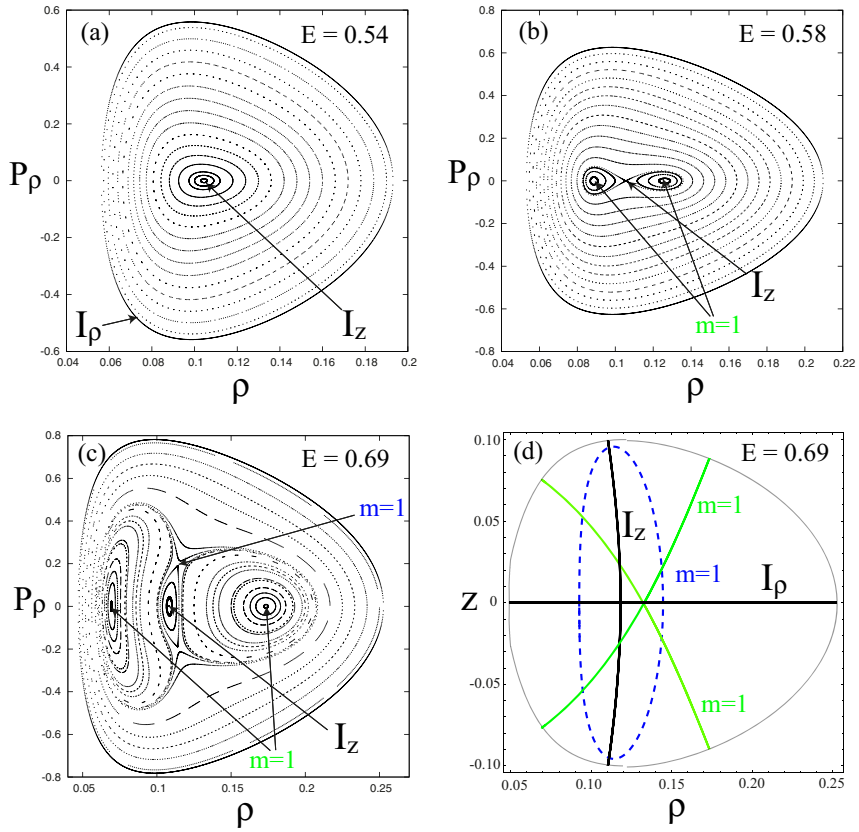

Fig. 6. (a)–(c) Surfaces of section for $p_z = 0$ illustrating the first and the second pitchfork bifurcations of the normal mode family I_z. (d) Stable (green lines) and unstable (dashed blue line) periodic motions of multiplicity $m = 1$ arisen from the first and the second bifurcations, respectively.

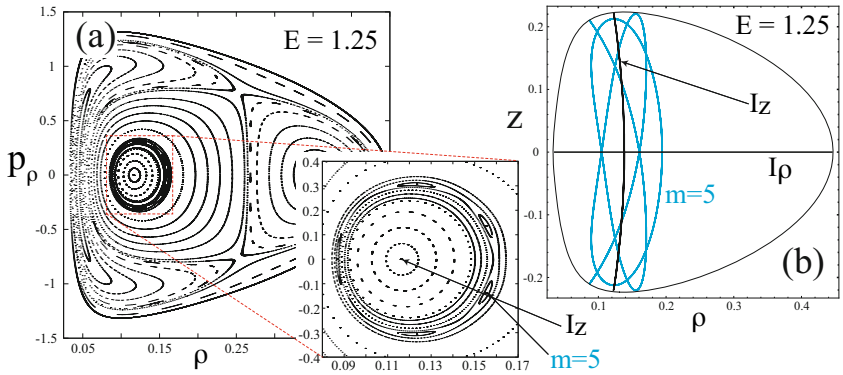

Fig. 7. (a) Surface of section $p_z = 0$ after the island-chain bifurcation of multiplicity $m = 5$ suffered by the normal mode I_z. (b) Cyan line represents the new stable periodic orbits that arises after the bifurcation. Both figures for energy $E = 1.25$.

.

For higher energy values, the dynamics is increasingly complex. In particular, for $E \approx 2.2431$ and $E \approx 2.3861$, the normal mode I_ρ suffers two consecutive period-doubling bifurcations (see Fig. 5c). In the first one, from I_ρ which becomes unstable, there appears a new stable orbit of multiplicity $m = 2$. In the second one, I_ρ again becomes unstable and it gives rise two new $m = 2$ unstable periodic orbits. These bifurcations can be observed in the $p_\rho = 0$ Poincaré maps of Figures 11a and 12a for $E = 2.26$ and for $E = 2.3862$, respectively. In Figure 11b and 12b are depicted the new periodic motions that appear after these bifurcations. It is worth notice that even at this high energy, most of the phase space remains regular. For energy values greater than $E = 2.4$, the behavior of the stability index of I_ρ is highly oscillatory (see Fig. 5d) and before the escape energy $E_{s1} \approx 2.4372$, this periodic orbit suffers several bifurcations which are not reflected in this study.

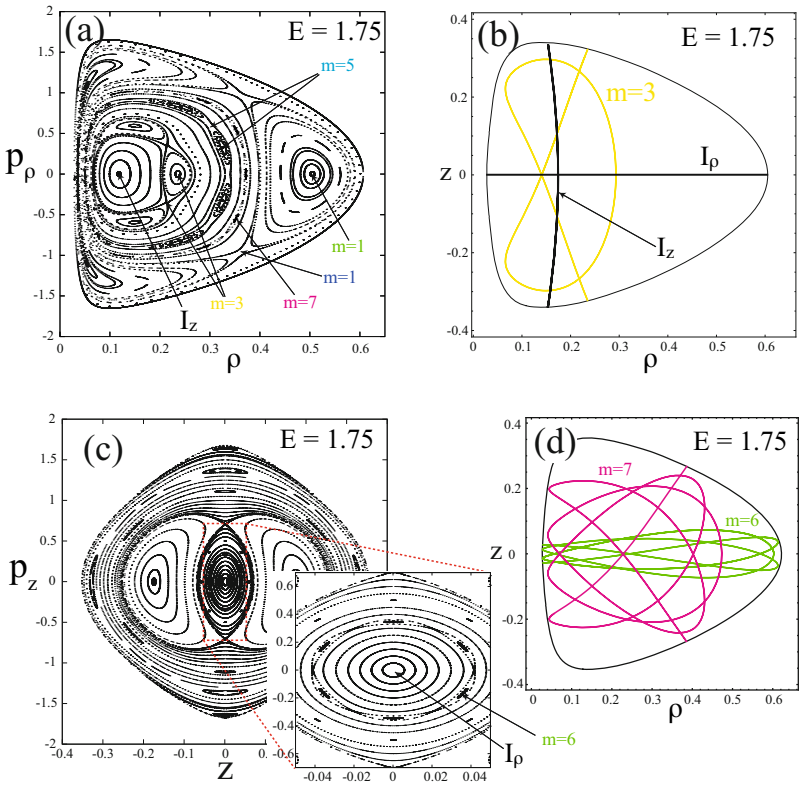

Fig. 8. (a) Surface of section $p_z = 0$ after the island-chain bifurcation of multiplicity $m = 3$ suffered by I_z. In this Poincaré section it is also possible to observe the $m = 7$ island-chain bifurcation suffered by I_z at $E \approx 1.0206$ (magenta lines in Fig. 5a). (b) The yellow line is the new stable periodic orbit that arises from the $m = 3$ island bifurcation. (c) $p_\rho = 0$ surface of section where it is observed the $m = 6$ island-chain bifurcation suffered by I_ρ at $E \approx 0.5200$ (green lines in Fig. 5b). (d) The magenta and green orbits are, respectively, the new stable periodic motions that arise from the $m = 7$ and $m = 6$ island bifurcations. See the text for details.

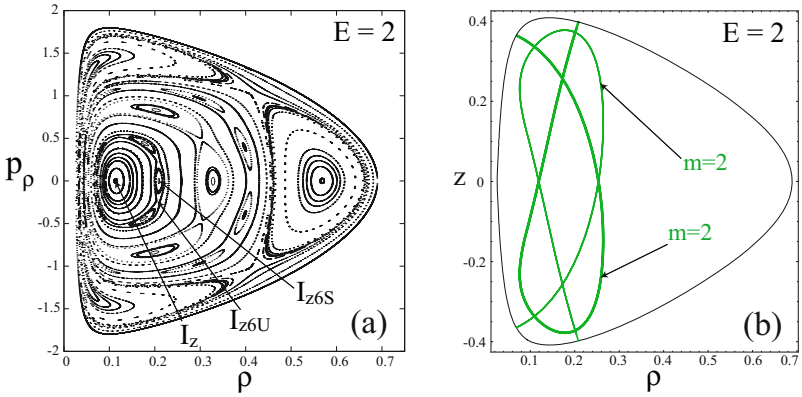

Fig. 9. (a) Surface of section $p_z = 0$ after the double period-doubling bifurcation suffered by I_z at $E \approx 1.8692$. (b) The dark green orbits are the two new stable periodic orbits of multiplicity $m = 2$ appearing after the bifurcation. All figures for energy $E = 2$.

5.3 Escape dynamics

When the energy approaches the trap depth energy given by $E_{s1} \approx 2.4372$, there is a big chaotic region around the periodic orbit I_ρ (see the surfaces of section of Fig. 13 for $E = 2.4371$). When the energy passes through the value $E_{s1} \approx 2.4372$, the first orbit to leave the trap is I_ρ as well as the nearest quasiperiodic orbits surrounding it because they are strongly oriented to the P_{s1} escape channel. This results in unbounded $p_z = 0$ surfaces of section (see Fig. 14a for $E = 2.5$). Furthermore, part of the chaotic sea around I_ρ disappears becoming a escape region visible as a "gap" in the Poincaré sections of Figure 14, in which only few points appear. These points correspond to orbits with initial conditions in the gap which remain trapped for a given time, crossing the surface of

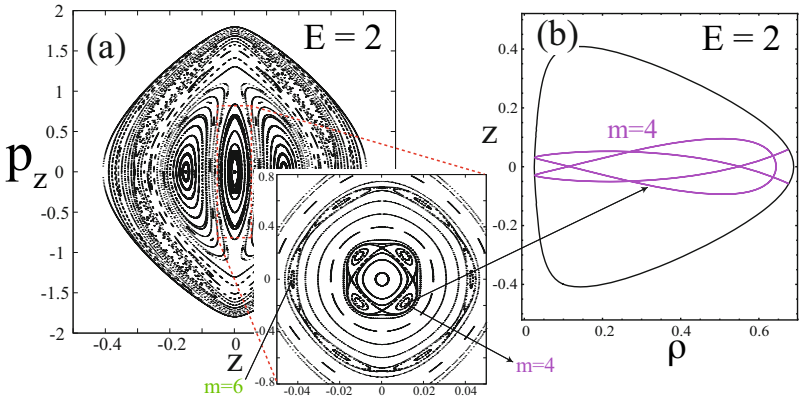

Fig. 10. (a) Surface of section $p_\rho = 0$ showing the resonance around I_ρ appearing after the $m = 4$ island-chain bifurcation of the normal mode family I_ρ at $E \approx 1.9135$. (b) The purple orbit is the stable $m = 4$ periodic orbit after the bifurcation. All figures for energy $E = 2$.

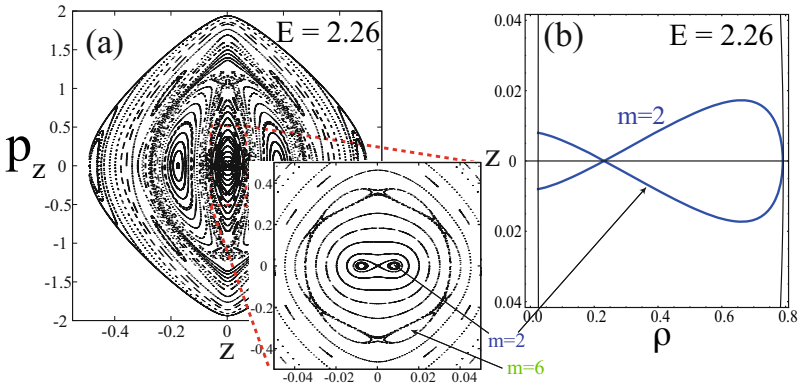

Fig. 11. (a) Surface of section $p_\rho = 0$ after the period-doubling bifurcation of the normal mode family I_ρ at $E \approx 2.2431$ (blue branch in Fig. 5c). (b) Stable $m = 2$ periodic orbit that arises after this period-doubling bifurcation. Both figures for energy $E = 2.26$ and for $p_\phi = 0.05$.

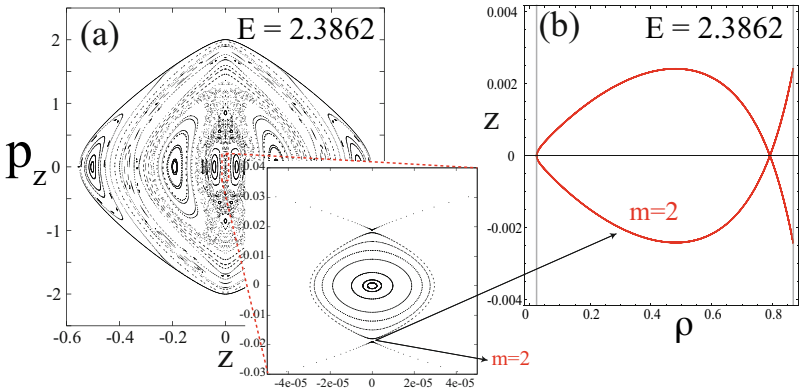

Fig. 12. (a) Surface of section $p_\rho = 0$ after the period-doubling bifurcation of the normal mode family I_ρ at $E \approx 2.3861$ (red branch in Fig. 5c). (b) Unstable $m = 2$ periodic orbit that appears after this period-doubling bifurcation. All figures for energy $E = 2.3862$ and for $p_\phi = 0.05$.

section a certain number of times before leaving the trap. An example of this kind of escape orbits is showed in Figure 14c. Note that, although $E > E_{s1}$, there are significant phase space regions which do not have access to the escape channel. Orbits living in these regions remain trapped forming robust KAM tori around stable periodic orbits.

When the energy is bigger than the threshold $E_{s2} \approx 2.5503$, the escape channel along the saddle point P_{s2} is also open, and I_z and the quasiperiodic motions around it are the first orbits to escape across P_{s2}. As consequence, the $p_\rho = 0$ sections are unbounded and this escape region appears as a new "gap" in the corresponding Poincaré sections (see Fig. 15 for $E = 2.75$).

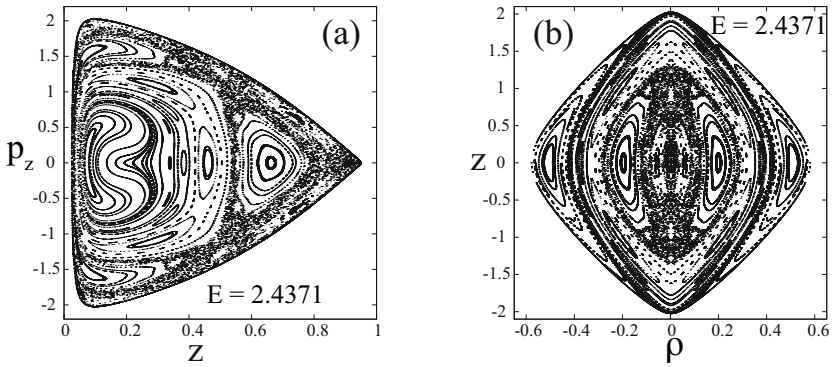

Fig. 13. Surfaces of section (a) $p_z = 0$ and (b) $p_\rho = 0$ for $E = 2.4371$. Both figures for energy $E = 2.4371$ and for $p_\phi = 0.05$.

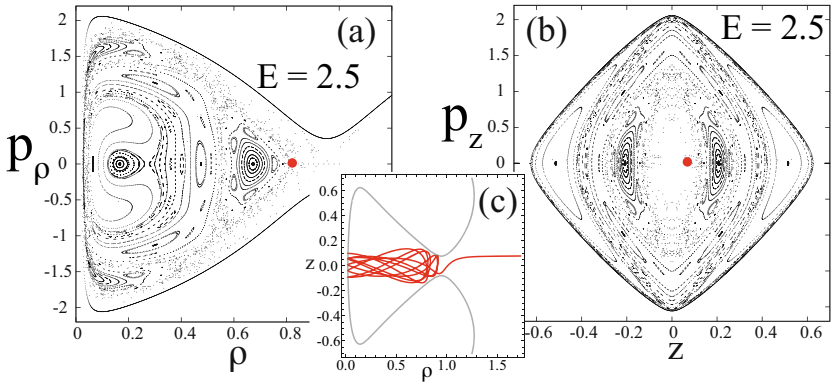

Fig. 14. Surfaces of section (a) $p_z = 0$ and (b) $p_\rho = 0$ for $E = 2.5$ and for $p_\phi = 0.05$. (c) Escape orbit. The initial conditions of this orbit are indicated with a red dot in the Poincaré sections.

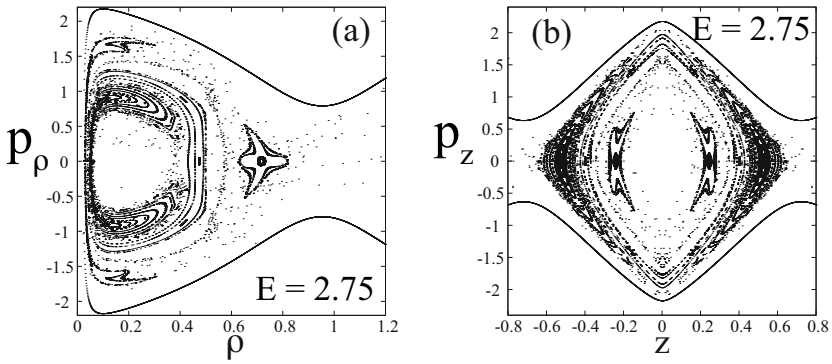

Fig. 15. Surfaces of section (a) $p_z = 0$ and (b) $p_\rho = 0$ for $E = 2.75$ and for $p_\phi = 0.05$.

As the energy grows, an increasing number of orbits have access to the escape channels and the unbounded and the chaotic regions in the surfaces of section grow in size. It is worth notice that even at high energy values, where most of the orbits are unbounded or chaotic, it is still possible to find regions of trapped regular motion. In particular, in the Poincaré sections of Figure 16 for $E = 3.5$ we observe that the islands around the $m = 1$ periodic orbits appearing after the first pitchfork bifurcation (green orbits in Fig. 6) are the last regions of bounded motion to survive at high energies.

6 Dynamics for $p_\phi = 0.5$

When $p_\phi = 0.5$, the minimum P_m of the effective potential $U(\rho, z; A')$ is located at $\rho_m \approx 0.43237$, its energy is $E_m \approx 1.86815$ and the saddle point energies are $E_{s1} \approx 2.57645$ and $E_{s2} \approx 3.69005$. Now, the centrifugal barrier is stronger and it pushes the trapping region far from the centre of the trap (see Fig. 3c). As in the previous section, we study the evolution of the phase space structure as the energy increases. We perform this study in a less comprehensive way than in Section 5, namely

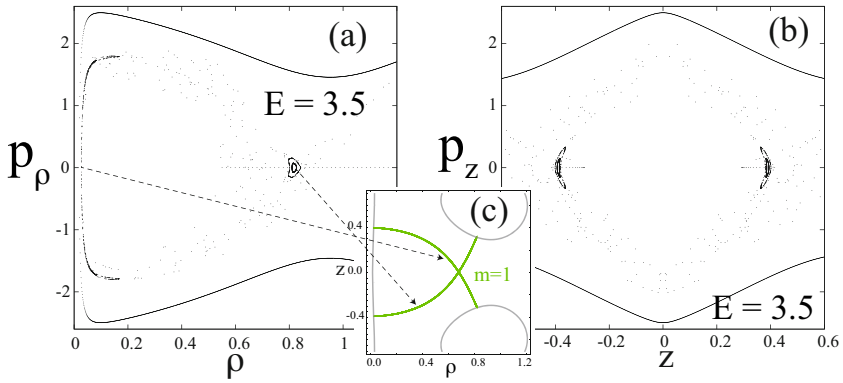

Fig. 16. Surfaces of section (a) $p_z = 0$ and (b) $p_\rho = 0$ for $E = 3.5$ and for $p_\phi = 0.05$.

only by using Poincaré sections. When the energy is close enough to $E_m \approx 1.86815$ (see Fig. 17a for $E = 2$), the $p_z = 0$ surface of section presents the same qualitative structure as Figure 4a, with the normal modes I_ρ and I_z ruling the dynamics. When the energy increases, the surfaces of section of Figure 17b for $E = 2.1$ and Figure 17c for $E = 2.2$ show that I_ρ and I_z suffer two consecutive pitchfork bifurcations. After these bifurcations, the phase space reaches the same structure as in Figure 6c. The phase space structure remains basically unchanged until the energy reaches the trapping threshold $E_{s1} \approx 2.57645$. Indeed, even for $E = 2.57$, a resonance coming form a $m = 2$ island bifurcation of I_ρ is the only remarkable change in the structure of the phase space (see Fig. 17d). Surprisingly and except for the two thin stochastic layers of chaotic motions in the separatrix regions, the system presents a regular KAM tori structure.

In the energy interval $E_{s1} \approx 2.57645 < E < E_{s2} \approx 3.69005$, the escape channel along the ρ direction opens and the $p_z = 0$ surfaces of section are unbounded because the quasiperiodic motions around I_ρ begin to escape (Figs. 17e–17f for $E = 2.8$ and $E = 3.5$). In these Poincaré sections we find a wide region of chaotic motion acting as a fuzzy border between bounded and unbounded motions.

When the energy is bigger than the saddle point energy $E_{s2} \approx 3.69005$, the escape channel along P_{s2} is already open and the quasiperiodic orbits around the I_z periodic orbit can also escape. Thence, the corresponding $p_z = 0$ surfaces of section have a hole in the central region (see Fig. 17g for $E = 3.7$). Large regions of chaotic orbits are also observed. As the energy is further increased, increasingly orbits escape, in such way that when $E = 4$ only a small region of confined orbits persists (see Fig. 17h). As in the previous case for $p_\phi = 0.05$, the islands around the $m = 1$ periodic orbits appearing after the first pitchfork bifurcation are the last regions of bounded motion to survive.

If we compare the behavior of the system for $p_\phi = 0.5$ to the behavior of the system for $p_\phi = 0.05$ (Sect. 5), we find that the dynamics in both cases is qualitatively very similar. In particular, in both cases the system suffers the same two pitchfork bifurcations that mark the beginning of the nonlinear behavior of the system.

7 Summary and conclusions

In this paper we carry out a systematic study of the classical dynamics of a neutral atom trapped in a magnetic quadrupole trap. In Sections 2 and 3, under the adiabatic approximation, the trapping potential and the Hamiltonian governing the dynamics of the system are stated. Due to the axial symmetry of the potential, the z component p_ϕ of the angular momentum is conserved. Thence, in cylindrical coordinates the Hamiltonian defines a two-degree of freedom dynamical system. After a convenient selection of units, the problem is seen to depend on two parameters: p_ϕ and the energy E. In Section 4, the energy and position of the critical points of the effective trapping potential $U(\rho, z; A')$ are studied as a function of p_ϕ. We find that the shape of $U(\rho, z; A')$ is determined by the presence of a minimum P_m and two saddle points P_{s1} and P_{s2}.

In Sections 5 and 6 and for two different values of p_ϕ, we carry out the numerical investigation of the phase space structure for increasing energy. By direct inspection of the equations of motion and using suitable Poincaré surfaces of section, we have found that two fundamental stable periodic orbits determine the phase space structure of the system. These basic periodic motions are the radial I_ρ and the axial I_z nonlinear normal modes of the system. In Section 5 for $p_\phi = 0.05$, the numerical continuation of families of periodic orbits allows us to compute the stability diagrams of the normal modes I_ρ and I_z as a function of the energy E. This investigation shows the presence of several bifurcations. Using Poincaré sections, some of those bifurcations as well as the new periodic orbits emanating from them, have been studied in detail. The increase of the energy has two main effects. One of them is that the phase space is constantly reorganizing around the new periodic orbits that appear after each bifurcation. The other one is that, as the energy approaches the trapping thresholds given by the energy of the saddle points P_{s1} and P_{s2}, the regularity of the system decreases because the phase space begins to be filled with regions of chaotic motions. For energy values above the trapping thresholds, the system dynamics is increasingly dominated by unbounded and by chaotic motions. However, even for energies above

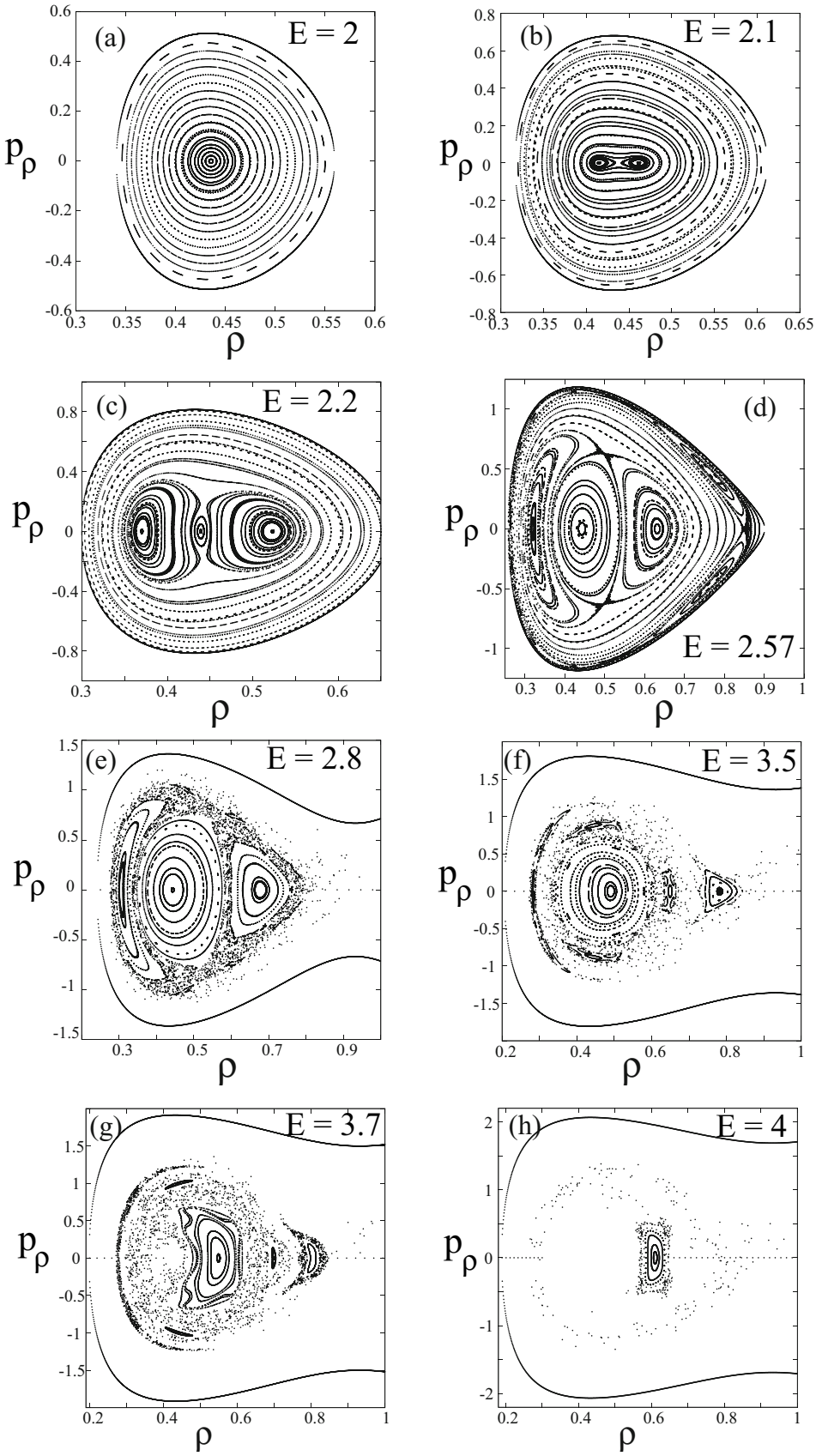

Fig. 17. Evolution as a function of the energy E of the $p_z = 0$ surfaces of section. All figures for $p_\phi = 0.5$.

the escape values, it is possible to find regions of regular trapped motion.

We noted in the Introduction the importance of knowing how the atoms move in the trap. However, to our knowledge, the present paper is the first exhaustive study of the classical dynamics of a magnetically trapped neutral atom. The extension of this study to atoms confined in different magnetic trap configurations as the Ioffe trap are now under consideration.

This work has been supported by the research projects MTM2011-28227-C02-02 (Spanish Ministry of Education and Science).

References

1. M.H. Anderson, J.R. Ensher, M.R. Matthews, C.E. Wieman, E.A. Cornell, Science **269**, 198 (1995)
2. K.B. Davis, M.-O. Mewes, M.R. Andrews, N.J. van Druten, D.S. Durfee, D.M. Kurn, W. Ketterle, Phys. Rev. Lett. **75**, 3969 (1995)
3. C.C. Bradley, C.A. Sackett, R.G. Hulet, Phys. Rev. Lett. **78**, 985 (1997)
4. W. Ketterle, D.S. Durfee, D.M. Stamper-Kurn, in *Proceedings of the International School of Physics*, edited by M. Inguscio, S. Stringari, C.E. Wieman (Societa Italiana Di Fisica, 1999), pp. 67–176
5. H.J. Metcalf, P. van der Straten, *Laser Cooling and Trapping* (Springer-Verlag, New York, 1999)
6. C. Monroe, E. Cornell, C. Wieman, in *Proceedings of the International School of Physics*, edited by E. Arimondo, W.D. Phillips, F. Strumia (North-Holland, Amsterdam, 1993), pp. 361–378
7. S. Chu, Rev. Mod. Phys. **70**, 685 (1998)
8. C.N. Cohen-Tannoudji, Rev. Mod. Phys. **70**, 707 (1998)
9. W.D. Phillips, Rev. Mod. Phys. **70**, 721 (1998)
10. K.B. Davis, M.O. Mewes, W. Ketterle, Appl. Phys. B **60**, 155 (1995)
11. W. Ketterle, N.J. van Druten, Adv. At. Mol. Opt. Phys. **37**, 181 (1996)
12. E. Majorana, Nuovo Cimento **9**, 43 (1932)
13. C.V. Sukumar, D.M. Brink, Phys. Rev. A **56**, 2451 (1997)
14. T. Bergeman, G. Erez, H.J. Metcalf, Phys. Rev. A **35**, 1535 (1987)
15. A.L. Migdall, J.V. Prodan, W.D. Phillips, T.H. Bergeman, H.J. Metcalf, Phys. Rev. Lett. **54**, 2596 (1985)
16. W. Paul, Rev. Mod. Phys. **62**, 531 (1990)
17. D.E. Pritchard, Phys. Rev. Lett. **51**, 1336 (1983)
18. V. Gomer, O. Harms, D. Haubrich, H. Schadwinkel, F. Strauch, B. Ueberholz, S. aus der Wiesche, D. Meschede, Hyperfine Interact. **109**, 281 (1997)
19. A.G. Martin, K. Helmerson, V.S. Bagnato, G.P. Lafyatis, D.E. Pritchard, Phys. Rev. Lett. **61**, 2431 (1988)
20. K. Helmerson, A. Martin, D.E. Pritchard, J. Opt. Soc. Am. B **9**, 483 (1992)
21. T. Bergeman, private communication
22. T. Bergeman, Bull. Am. Phys. Soc. **31**, 939 (1986)
23. E.L. Surkov, J.T.M. Walraven, G.V. Shlyapnikov, Phys. Rev. A **49**, 4778 (1994)
24. W.R. Smythe, *Static and Dynamic Electricity* (McGraw-Hill, New York, 1950)
25. A. Weinstein, Inventiones Math. **20**, 47 (1973)
26. J.P. Ortega, Proc. Roy. Soc. Edinburgh Sect. A **133**, 665 (2003)
27. S. Wiggins, *Global Bifurcations and Chaos: Analytical Methods* (Applied Mathematical Sciences, Springer-Verlag, New York, 1988)
28. R. Barrio, F. Blesa, Chaos Solitons Fractals **41**, 560 (2009)
29. K.R. Meyer, G.R. Hall, *Introduction to Hamiltonian Dynamical Systems and the N-body Problem* (Applied Mathematical Sciences, Springer-Verlag, New York, 1992)
30. M. Lara, J.P. Salas, Chaos **14**, 763 (2004)
31. M. Iñarrea, V. Lanchares, J.F. Palacián, A.I. Pascual, J.P. Salas, P. Yanguas, Phys. Rev. A **76**, 052903 (2007)
32. F. Blesa, J. Mahecha, J.P. Salas, M. Iñarrea, Phys. Lett. A **374**, 191 (2009)
33. M. Iñarrea, J.F. Palacián, A.I. Pascual, J.P. Salas, J. Chem. Phys. **135**, 014110 (2011)
34. F.J. Muñoz-Almaraz, E. Freire, J. Galán, E. Doedel, A. Vanderbauwhede, Physica D **181**, 1 (2003)
35. W.H. Wing, Prog. Quantum Electron. **8**, 181 (1984)
36. P. Meystre, *Atom Optics* (Springer-Verlag, New York, 2001)